

# GOODS-*Herschel* data release

September 7, 2012

## 1 Introduction

GOODS-*Herschel* is an ESA open time key program (PI D. Elbaz, total time 361.3 hours, described in Elbaz et al. 2011, A&A 533, 119) consisting of the deepest *Herschel* far-infrared observations of the two Great Observatories Origins Deep Survey (GOODS) fields in the Northern and Southern hemispheres.

The full  $10' \times 16'$  GOODS-North field has been imaged with PACS at 100 and  $160 \mu\text{m}$  and SPIRE at 250, 350 and  $500 \mu\text{m}$ . By construction, the SPIRE images encompass the GOODS-N field proper but also cover a wider area that is included in the FITS images of the present data release but not in the catalogs due to the lack of deep  $24 \mu\text{m}$  priors for *Herschel* source extraction (see section 3). The total observing time in GOODS-N is 124 hours and 31.1 hours for PACS and SPIRE, respectively.

A smaller area within GOODS-S, covering about  $10' \times 10'$  (but reaching the deepest sensitivity over  $\sim 64 \text{ arcmin}^2$ ) has been imaged for a total of 206.3 hours in order to integrate five times longer per unit sky position and to reach the confusion limit at  $100 \mu\text{m}$  with PACS of 0.7 mJy ( $3\sigma$ ).

This data release includes the GOODS-*Herschel* images, as well catalogs of point source detections with significance  $> 3\sigma$ . Since IRAC  $3.6 \mu\text{m}$  prior positions were used to determine the MIPS  $24 \mu\text{m}$  source positions at which PSF-fitting source extraction was performed in the *Herschel* images, we also include the *Spitzer* IRAC and MIPS photometry for the *Herschel* sources in the catalogs. The data from 3.6 to  $70 \mu\text{m}$  come from two *Spitzer* Legacy Programs (PI: M. Dickinson): IRAC and MIPS  $24 \mu\text{m}$  from GOODS, and MIPS  $70 \mu\text{m}$  from the Far-Infrared Deep Extragalactic Legacy (FIDEL) survey, the latter incorporating additional  $70 \mu\text{m}$  observations by Frayer et al. (2006).

The images and catalogs from this GOODS-*Herschel* data release are available from the *Herschel* Database in Marseille (HeDaM), at <http://hedam.oamp.fr/GOODS-Herschel>.

## 2 Map creation

### 2.1 PACS maps

The GOODS-H observations were executed in the scan-technique with the PACS photometer on board of the *Herschel* Space Observatory (Pilbratt et al. 2010). The scan maps were performed by slewing the spacecraft at a constant speed of 20 arcsec/sec along parallel lines. During the full scan-map duration the bolometers were constantly read-out at 40 Hz. However, due to satellite data-rate limitations, on-board reduction and compression steps are necessary before the data are down-linked. In the GOODS-H observations, taken in the PACS prime mode, four subsequent frames were averaged in both bands for a final sampling rate of 10 Hz.

The data were reduced within the HIPE environment in the *Herschel* Common Science System (HCSS) with the official PACS Photometer pipeline (Wieprecht et al. 2009). The first steps of the pipeline consist of identifying functional blocks in the data, flagging bad pixels, flagging any saturated data, converting detector signals from digital units to volts, flat-fielding and flux calibrating the data. Short glitches in the detector timelines are flagged and interpolated with an HCSS implementation of the multiresolution median transform, developed by Starck & Murtagh (1998). After adding the instantaneous pointing information (coordinates of the reference pixel and position angle) to PACS timelines, we apply recentering corrections on the base of  $24\ \mu\text{m}$  prior positions, as explained in Lutz et al. (2011).

The main source of noise in the PACS data is the so-called  $1/f$  noise, with spectral density of the form  $S(f) = 1/f^\alpha$ , where  $f$  is frequency. The  $1/f$  noise of the PACS photometer is roughly  $\propto f^{-0.5}$  over the relevant frequencies. The *Herschel* PACS pipeline in the “deep cosmological survey” scientific case removes the  $1/f$  noise with a high-pass filtering method. Specifically, the  $1/f$  noise is removed by filtering the timeline with a running box median filter with a size expressed in detector readouts, and then subtracting the median-filtered timeline from the original data. The presence of a source within the filtering box boosts the median, thus leading to over-subtraction of part of the source flux. This can be overcome by properly masking the sources on the timeline to exclude readouts corresponding to the source when estimating the median. Simulations performed by the PACS ICC (Popesso et al. in preparation) show that a masking strategy using circular patches placed on prior source positions is the best solution to reduce the amount of flux loss due to the high-pass filtering and to preserve flux-independence of the high-pass filtering effect over a large part of the flux range for detected sources. Following this result, we mask with a circular patch radius of 4 arcsec and 6 arcsec at 100 and 160  $\mu\text{m}$ , respectively, at the position of *Spitzer* 24  $\mu\text{m}$  sources with flux densities larger than 60  $\mu\text{Jy}$ . This allows us to mask almost the totality of the PACS detections. Three slightly extended objects in the GOODS-S map are masked with larger patches with 10 arcsec radius to remove strong high-pass filtering residuals. We choose a running box median filter with a half-width of 12 samples (24 arcsec) at 100  $\mu\text{m}$  and 20 samples (40 arcsec) at 160  $\mu\text{m}$ . This choice of the high-pass filter radius allows us to subtract as much as possible  $1/f$  noise, thus reducing the final map noise, without damaging the PACS PSF. We take into account the flux loss due to the high-pass filtering by applying a correction factor corresponding to our parameter settings (circular patch size and high-pass filter radius) provided in Popesso et al. (in preparation), 13% and 11% at 100 and 160  $\mu\text{m}$  respectively. For unmasked sources, in principle a larger correction factor should be applied; simulations suggest that this should be of order 20% (see Popesso et al. in preparation for the details). However, in practice, the measured fluxes for unmasked sources generally have quite low signal to noise ratios, and therefore the difference between the correction for masked and unmasked sources (approx. 8%) is essentially irrelevant relative to the noise for measurements of individual sources. In the GOODS-H source catalogs provided here, we have applied uniform correction factors regardless of whether the sources were masked or unmasked during the PACS low-pass filtering (see section 3).

Maps are created from the timelines for each AOR via the HCSS photProject algorithm, which is equivalent to the drizzle method (Fruchter & Hook 2002). Each individual AOR map is projected with the same world coordinate system (WCS). We use pixel scales of 1.2 arcsec and 2.4 arcsec for the 100  $\mu\text{m}$  and 160  $\mu\text{m}$  maps, respectively. These significantly oversample the PSF full width at half-maximum (FWHM, 6.7 arcsec and 11 arcsec for the 100  $\mu\text{m}$  and 160  $\mu\text{m}$  passbands, respectively), by factors of 5.6 and 4.6, respectively,

corresponding to twice smaller pixels than the Nyquist sampling; the  $100\ \mu\text{m}$  pixel scale was chosen to be equal to that used for the  $24\ \mu\text{m}$  maps produced by the GOODS team and the pixel scales of the larger wavelength PACS and SPIRE bands were chosen to be integer multiples of this reference pixel scale. Given the high data redundancy in these deep fields, PSF widths and noise correlation in the final map can be reduced by choosing projection “drops” that are smaller than the physical PACS pixel size. The drop size is defined by the *pixfrac* parameter, which is the ratio between drop and input detector pixel size. We set *pixfrac* to 0.06 given the extremely high data redundancy. The final map is obtained by coadding all individual AOR maps, weighting the individual maps by the effective coverage of each pixel. The final error map is computed as the error of the weighted mean. The error maps have slightly larger values near the positions of PACS sources, probably due to small, residual jittering in the scan alignments.

The final coverage map is the sum of all individual AOR coverages. Since we use a drizzle method, the coverage is obtained as shown in Eq. 2 in Fruchter & Hook (2002). The coverage values are not the amount of time spent on sky pixel, but rather the sum of the fractional drop areas contributing to the sky pixel flux.

## 2.2 SPIRE maps

The SPIRE observations of GOODS-H were executed as cross-linked scan maps with the SPIRE photometer (Griffin et al. 2010). The three SPIRE bolometer arrays cover band-passes with  $\lambda/\Delta\lambda \sim 3$  centered at 250, 350 and  $500\ \mu\text{m}$ . The bolometers do not fill the field of view, which means that scanning at a particular angle is necessary in order to provide relatively homogeneous coverage. There are two possible scan angles with SPIRE, at almost orthogonal scan directions (84.8 deg). Combining both scan directions is possible in a single observation, using the so-called cross-linked maps. At each scan direction the telescope scans the sky at a constant speed of  $30''/\text{s}$  and the bolometer signals are read at 18 Hz. To achieve better sensitivity the cross-linked scan maps are repeated a number of times.

Each single GOODS-H SPIRE cross-linked map covers  $22' \times 19'$  with 3 repetitions, and we implement a 19-point dithering strategy, first introduced for SPIRE maps by the HerMES team (Oliver et al. 2012). The centers of the maps, all with the same geometry and number of repetitions, are offset in such a way so that the coverage in the central part is very flat and much more homogeneous than a single cross-linked map (see SPIRE Observers’ Manual for more details). The dithering also allows the maps to be generated using a smaller pixel size without affecting the homogeneity of the coverage. To achieve the required GOODS-H depth in the SPIRE bands, we repeated the 19-point dithering scheme twice, which makes 38 single cross-linked SPIRE maps<sup>1</sup>.

The data from all 38 maps were processed with HIPE version 6 with calibration version SPIRE\_CAL\_5\_0. We have used the standard SPIRE photometer pipeline (Griffin et al. 2008); the only deviation is that we have used an alternative glitch removal technique – the Sigma-Kappa deglitcher – which is available in HIPE. We found that in most cases for extragalactic fields without any strong emission (extended structure or bright point sources) this alternative method is more robust in comparison to the default wavelet deglitcher. The SPIRE standard map-making technique is the naive projection, where the signals of all bolometers falling in a given sky pixel are averaged. Due to the low  $1/f$  noise knee in the SPIRE data (see Griffin et al. 2010), the quality of these maps is sufficient

---

<sup>1</sup>For one of the 38 maps we had to reduce the repetitions from 3 to 2 in order to stay within the allocated time

and comparable to, if not better than, more sophisticated techniques like MADMap or Sanepic. Prior to the naive projection of the timeline fluxes, a median baseline is removed on a scan-by-scan basis. As there are no strong and extended source in the GOODS-N field, the median baseline removal performs very well and provides baselines that are very close to zero. We visually screened each of the 38 SPIRE maps for any possible missed glitches or other map imperfections, and we checked for astrometry offsets with respect to catalogs at shorter wavelengths, notably MIPS  $24\ \mu\text{m}$ . The astrometry offsets of all 38 maps were well within the *Herschel* absolute pointing error of  $\sim 1''$  (see Pilbratt et al. 2010). Finally, all median baseline-removed bolometer timelines from all 38 observations were used in the naive map making for the final GOODS-N maps at  $250\ \mu\text{m}$ ,  $350\ \mu\text{m}$  and  $500\ \mu\text{m}$ . The pixel sizes we used for the final SPIRE maps are 3.6, 4.8 and 7.2 arcsec. Although these pixel sizes are about twice smaller than the Nyquist sampling for the corresponding beam FWHM (the PSF FWHM for the SPIRE passbands is 18.2 arcsec, 24.9 arcsec and 36.3 arcsec for the  $250\ \mu\text{m}$ ,  $350\ \mu\text{m}$  and  $500\ \mu\text{m}$  passbands, respectively), the maps look much cleaner; having more pixels in the beam also helps the deblending.

### 2.3 Differences between the PACS and SPIRE maps

We wish to stress that the PACS and SPIRE photometric maps are not calibrated in the same way, hence users should proceed differently when using one or the other type of data to extract point source flux densities. We discuss below the two differences that should be considered before performing point source photometry.

The first difference concerns the units used in the PACS and SPIRE images. Pixel values in the SPIRE images are given in units of Jy/beam, whereas they are instead provided in Jy for PACS. This implies that the central pixel of a point source in a SPIRE image measures its integrated flux density. When PSF-fitting is used to measure flux densities for individual sources in the SPIRE maps, no aperture correction is necessary because of the unit definition; the source flux is defined by the peak value of the fitted PSF. For PACS, instead, flux densities of point sources are measured as the sum of all pixel values (in Jy) associated with the source. When a PSF with finite radius is fit to the image, we apply an aperture correction factor as discussed in Section 3.

The second difference is related to the background level definition. SPIRE images were constructed after subtracting a fixed background level so as to remain with a zero mean intensity in the images. As a result, the histogram of pixels peaks at a negative value (see Fig. 1). For PACS instead, the reduction procedure does not subtract a constant value, and the net background level is approximately (if not exactly) zero. When generating source catalogs and measuring fluxes, we use essentially the same methods to evaluate the net background for both the PACS and SPIRE data. Mock sources spanning a large range of flux densities were added to the images, and flux densities were extracted for these sources. An effective background level was derived that achieves consistency between the input fluxes and the measured fluxes. This background is slightly positive for PACS and negative for SPIRE.

## 3 Source Extraction

At the resolution of *Spitzer* and *Herschel*, ranging from 5.7 (MIPS- $24\ \mu\text{m}$ ) to 36.3 arcsec (SPIRE- $500\ \mu\text{m}$ ) FWHM, most of the objects detected in our data are point sources. Therefore, to produce photometric measurements we used a PSF-fitting technique that takes into account, as prior information, the expected position of the sources (Magnelli

et al. 2009, 2011). Starting from a catalog of IRAC source positions from the GOODS *Spitzer* Legacy Program (PI: M. Dickinson), we first extract sources at  $24\ \mu\text{m}$ , and then use the  $24\ \mu\text{m}$ -detected sources as priors for the following extraction of point sources in the *Spitzer*  $70\ \mu\text{m}$  and *Herschel* images.

The IRAC catalogs were generated by the GOODS-*Spitzer* team using SExtractor (Bertin & Arnouts 1996). Sources were detected in a weighted average of the  $3.6\ \mu\text{m}$  and  $4.5\ \mu\text{m}$  images, using a ‘Mexhat’ convolution kernel to enhance deblending in crowded regions. Nevertheless, the width of the IRAC PSF strongly inhibits the ability to distinguish sources separated by less than about  $4''$ . In such cases, objects will tend to be blended into a single detected source in the IRAC catalogs. For the purpose of *Spitzer* and *Herschel* source extraction, this implies that there will rarely be IRAC priors separated by less than  $4''$ , or roughly 2/3rds of the FWHM of the *Spitzer*/MIPS beam size at  $24\ \mu\text{m}$  or that of *Herschel*/PACS at  $100\ \mu\text{m}$ . When two objects are blended into a single detection in the IRAC catalog, the centroid position of the blended source may be significantly offset from the true positions of the individual components.

Given prior information about the expected positions of sources, we fit empirical PSFs to the mid- and far-infrared maps. First, we fit PSFs to the *Spitzer* MIPS  $24\ \mu\text{m}$  images at the positions of all sources detected in the IRAC catalog. The flux of each source is determined from the scaled intensity of the fitted PSF. Groups of nearby sources whose PSFs would overlap are fit simultaneously in order to deblend their fluxes. Uncertainties are also estimated following the procedure described in section 4 below. Then, based on the list of  $24\ \mu\text{m}$  detections with signal-to-noise ratio  $S/N > 3$ , we extract fluxes from the  $70$ ,  $100$ ,  $160$ ,  $250$ ,  $350$  and  $500\ \mu\text{m}$  images in the same manner. This method deals with a large part of the blending issues encountered in crowded fields and allows straightforward multi-wavelength association between near-, mid- and far-infrared sources.

One potential drawback of this method is that we must assume that all sources present in our  $24\ \mu\text{m}$  images are detected at IRAC wavelengths, and that all far-infrared sources are detected at  $24\ \mu\text{m}$ . Based on the relative depth of our near-, mid- and far-infrared images, and on a careful analysis of the infrared SEDs of galaxies, Magnelli et al. (2011) and Magdis et al. (2011) have shown that this assumption is true, even in the case of our deep GOODS mid- and far-infrared images. Only a very small number of *Herschel* sources are undetected at  $24\ \mu\text{m}$ , largely because of strong silicate absorption (e.g., at  $9.7\ \mu\text{m}$  rest frame) that causes them to “drop out” of the MIPS data.

For PACS, empirical PSFs were constructed by stacking isolated point like objects present in the mosaics. For the MIPS and PACS data, the empirical PSFs have a finite extent and do not include the totality of the power located in the source wings. Therefore a flux correction is applied, as would be done for a standard aperture flux measurement. For the *Spitzer* observations, the aperture corrections were taken from the *Spitzer* Data Handbook, while for the *Herschel*-PACS observations they were derived by comparing our empirical PSFs with the reference in-flight PSF for our observing mode (scan map with speed  $20\ \text{arcsec/sec}$ ) obtained from the observations of the asteroid Vesta (Berta et al. 2010, 2011). The *Herschel*-PACS empirical PSFs were kindly created by S. Berta, and are included with this data release. For PACS  $100\ \mu\text{m}$  PSFs the aperture corrections, defined as the fraction of total flux density contained within the empirical PSFs, are 0.6635 and 0.6702 for the GOODS-N and GOODS-S fields, respectively. For  $160\ \mu\text{m}$ , the respective aperture corrections are 0.6817 and 0.6991. Because of effects of high-pass filtering in the PACS data, additional corrections, of order 12%, must be applied to the flux measurements (see Section 2.1). These are already included in the catalogs provided with this data release.

We used the model PSF available from the Herschel Science Center to produce photometric measurements with SPIRE. These PSFs were resampled to the pixel scale of the GOODS-*Herschel* maps and broadened slightly by Gaussian convolution to match the FWHM measured from individual sources in the GOODS maps. Aperture corrections are not needed here because the SPIRE maps are calibrated in Jy/beam, as described in section 2.3.

For GOODS-N, the mid- and far-infrared images cover the full area field (approximately  $10' \times 16'$ ) with roughly uniform depth. The noise level in these data is homogeneous over most of that sky area, with some degradation near the edge where the exposure time is somewhat reduced. In the GOODS-S field the situation is different. While at  $24 \mu\text{m}$  the noise level is roughly uniform throughout image, the depth of our *Herschel* far-infrared observations in GOODS-S varies within the field. The deepest MIPS- $70 \mu\text{m}$  data in GOODS-S, with noise similar to those in GOODS-N for the same band, are limited to a region approximately  $10' \times 10'$  in extent. The outer regions of the GOODS-S field have somewhat shallower MIPS- $70 \mu\text{m}$  data, with noise that is larger by  $\sim \sqrt{2}$ ). The ultra-deep GOODS-*Herschel* PACS observations in GOODS-S (at  $100 \mu\text{m}$  and  $160 \mu\text{m}$ ) have uniform exposure time (with some degradation near the edges), but are limited to a region approximately  $10' \times 10'$  in extent which overlaps the deepest MIPS- $70 \mu\text{m}$  data. Finally, the GOODS-S field has not been observed with SPIRE as part of the GOODS-*Herschel* open time key program. The HerMES guaranteed time program (Oliver et al. 2012) obtained SPIRE observations of GOODS-S and the surrounding extended Chandra Deep Field South, but these are not incorporated into the present data release.

Although exposure times vary within our field, this data release provides the complete 24, 70, 100, 160, 250, 350 and  $500 \mu\text{m}$  source catalogs of the GOODS fields, i.e., we do not restrict the catalogs to regions with homogeneous coverage in all our mid- and far-infrared bands. For each IRAC prior position, we provide the exposure time or coverage value for the maps in each of the mid- and far-infrared bands that are available for each field. To obtain a sample that corresponds to a region with relatively homogeneous exposure time and sensitivity, the user should select only sources with coverage/exposure values greater than those quoted in the 2nd column of Table 1. We note that flux uncertainties estimated from residual maps (i.e.,  $\sigma^{ima}$ ; see Section 4) take into account the variation of the exposure time across our fields. Instead, uncertainties derived using Monte-Carlo simulations (i.e.,  $\sigma^{sim}$ ; see Section 4) were computed only for the regions with homogeneous exposure time, and hence are not provided for sources located outside those regions.

Flux calibration factors for the *Spitzer* 24 and  $70 \mu\text{m}$  data are derived from stars, assuming an in-band SED of a 10 000 K blackbody function (i.e.,  $F_\nu \propto \nu^2$ ; see the *Spitzer* data handbook for more details). On the other hand the PACS and SPIRE data are calibrated assuming an in-band SED of  $\nu F_\nu = \text{constant}$  (see the *Herschel* data handbook for more details). In either case, actual in-band SEDs for distant galaxies may be very different from those assumed for the instrument flux calibration. Hence, color-corrections may need to be applied to the flux density measurements reported in these catalogs. Because these color-corrections may depend on the redshifts and spectral properties of sources, we do not apply them in the released catalogs.

Finally, we note here that the released MIPS  $24 \mu\text{m}$  catalogs are slightly different than those published by Magnelli et al. (2011), in part due to the use of different IRAC prior catalogs. Here the catalogs of IRAC priors were generated in the same way for both GOODS fields, whereas in Magnelli et al. (2011) we used a different catalog for GOODS-S (from SIMPLE, Damen et al. 2011).

## 4 Noise estimates

The data used here come from the deepest mid- and far-infrared observations taken by the *Spitzer* and *Herschel* Space Observatories, which were designed to reach the confusion limit of these telescopes. Flux uncertainties are therefore a complex combination of photon and confusion noise. In order to estimate these flux uncertainties, and to characterize the quality of our catalogs, we use two different approaches. First, we compute the noise of each detection using our residual maps. Second, we estimate a statistical flux uncertainty based on Monte-Carlo simulations.

The noise values estimated from the residual maps are determined locally for every source. The residual map is generated by subtracting all individually-detected sources from the original image, and then is convolved with the PSF. The dispersion of pixel values in the convolved residual map is measured in a square region around each source, whose size in each dimension is ten times the PSF FWHM. This provides an estimate of the local noise level. This method has the advantage of taking into account the local noise variations in the map (and thus inhomogeneities in the exposure time), the quality of our fitting procedure, and a part of the confusion noise left in our residual maps (i.e., confusion noise due to sources fainter than the detection limit that are still present in the residual image). These noise estimates are given in our released catalogs as  $\sigma^{ima}$ .

In order to estimate the effect of confusion noise we performed extensive Monte-Carlo simulations. We added artificial sources to our images with a flux distribution that approximately matches the measured number counts (Papovich et al. 2004; Frayer et al. 2006; Berta et al. 2010, 2011; Oliver et al. 2010). To preserve the original statistics of the image (especially the crowding properties), only a small number of artificial objects was added to the image at a time. We then carried out the source extraction process following the method based on prior positions described above, and compared the resulting photometry to the input values. This process was repeated a large number of times using different source positions to improve the statistics, for a total of 20 000 artificial objects per field. The results of these Monte-Carlo simulations for our PACS and SPIRE observations are shown in Figures 2 and 3. For the MIPS 24  $\mu\text{m}$  and 70  $\mu\text{m}$  data, results of the analogous Monte-Carlo simulations are shown in Figure 1 of Magnelli et al. (2009).

Three important quantities were derived from these Monte-Carlo simulations : the photometric accuracy, the completeness, and the contamination of our catalogs as a function of flux density. Completeness is defined as the fraction of simulated sources extracted with a flux accuracy better than 50%. Contamination is defined as the fraction of simulated sources introduced with  $S < 2\sigma^{ima}$  that are extracted with  $S > 3\sigma^{ima}$ . Table 1 summarized these quantities.

Flux uncertainties derived from these Monte-Carlo simulations are denoted by  $\sigma^{sim}$ . These flux uncertainties have the advantage of accounting for nearly all sources of noise, which explains why they might be larger than noise estimates based on residual maps (i.e.,  $\sigma^{ima}$ ). However, this noise estimate is computed statistically for the whole image, not locally at the position of individual sources. In some cases, local effects can dominate the noise, for example when the exposure time is reduced near the edges of the maps, or when two sources are closely blended. These local effects, together with the background fluctuations due to the photometric confusion noise (i.e., the noise due to sources fainter than the detection limit that were not subtracted from the image to produce the residual map), is better taken into account by the noise estimated from the residual maps, which is estimated locally. **To be conservative, users should adopt the larger value of the uncertainty, choosing between  $\sigma^{ima}$  and  $\sigma^{sim}$ , but *not* the quadratic combi-**

**nation of both since they are not independent.** Finally, we remind the reader that the Monte-Carlo simulations were carried out over regions with relatively homogeneous exposure time (see 2nd column of Table 1). Therefore, uncertainties derived using these Monte-Carlo simulations are not suitable, and hence are not provided, for sources situated outside these homogeneous exposure time regions.

## 5 Clean index

A major source of uncertainty, particularly for the SPIRE data, comes from the high source density relative to the beam size, i.e., the so-called confusion limit (see Condon 1974). In the source catalogs provided in this data release we report  $3\sigma$  detections at all wavelengths, but we warn users that some of these sources may be affected by imperfect deblending with neighboring sources. In order to address this concern, we provide an estimator of the purity of the sources, labeled the “clean index,” which was used in Hwang et al. (2010) and Elbaz et al. (2010, 2011) to identify individual sources with the least probable contamination by bright neighbors. The clean index for a source results from the combination of the number of bright neighbors that it has in each of the *Herschel* bands observed - i.e., 100 and 160  $\mu\text{m}$  in both fields and 250, 350, 500  $\mu\text{m}$  in GOODS-North only - and in the *Spitzer* MIPS 24  $\mu\text{m}$  passband. For the purpose of computing the clean index, we define a “bright neighbor” to be a source brighter than half the flux density of the source of interest, and closer than  $1.1 \times \text{FWHM}$  of the PSF in each of the *Herschel* bands. The FWHM values of the *Herschel* PSFs are 6.7, 11, 18.2, 24.9, and 36.3 arcsec at 100, 160, 250, 350, and 500  $\mu\text{m}$  respectively. At 24  $\mu\text{m}$ , bright neighbors with  $F_{24} > 50\%$  of the central 24  $\mu\text{m}$  source are considered within a distance of 20 arcsec, corresponding to  $1.1 \times \text{FWHM}(250 \mu\text{m})$ . This number has been found from simulations to represent an efficient reference for the definition of clean areas where sources may be detected with reliable *Herschel* measurements.

The clean index provided in the last column of the catalogs was computed from the numbers of bright neighbors at 24, 100, 160, 250, 350 and 500  $\mu\text{m}$  - labeled Neib24, Neib100, Neib160, Neib250, Neib350 and Neib500 - in GOODS-North:

$$\begin{aligned} \text{clean\_index} = & \text{Neib24} + \text{Neib100} \times 10 + \text{Neib160} \times 100 \\ & + \text{Neib250} \times 1000 + \text{Neib350} \times 10000 + \text{Neib500} \times 100000 \end{aligned} \quad (1)$$

In GOODS-South, it was computed using the neighbors at 24, 100 and 160  $\mu\text{m}$ , which is equivalent to assuming that  $\text{Neib250} = \text{Neib350} = \text{Neib500} = 0$  in this field with no SPIRE observations from GOODS-*Herschel*:

$$\text{clean\_index} = \text{Neib24} + \text{Neib100} \times 10 + \text{Neib160} \times 100 \quad (2)$$

To take the most conservative approach to the potential effects of neighbors on the photometric accuracy of a given source, one may consider only sources with a  $\text{clean\_index} = 0$ . However, allowing Neib24 to be  $\leq 1$ , i.e., accepting at most one bright neighbor at 24  $\mu\text{m}$  within 20 arcsec, provides a relatively robust selection of clean measurements for almost 80% of the sources above the  $3\sigma$  detection limit in the *Herschel* bands. In Elbaz et al. (2011), an intermediate criterion was used, with  $\text{Neib24} \leq 1$  and  $\text{Neib}_\lambda \leq 0$  in all *Herschel* bands. The clean index should be considered here as a flag providing some insight on the purity of the measurements in the *Herschel* bands for a given source, but not as a strict quality flag that can be used blindly. Users are advised to check this clean index value especially when using the SPIRE measurements. A forthcoming paper (Leiton et al., in prep.) will discuss this index in more detail.

One can retrieve the number of 'bright' neighbors at each wavelength with the following expressions in IDL:

```
neib24=strmid(clean_index,'0',/reverse)
neib100=fix(strmid(clean_index,'1',/reverse)/10.)
neib160=fix(strmid(clean_index,'2',/reverse)/100.)
neib250=fix(strmid(clean_index,'3',/reverse)/1000.)
neib350=fix(strmid(clean_index,'4',/reverse)/10000.)
neib500=fix(strmid(clean_index,'5',/reverse)/100000.)
```

## 6 Format of the released catalogs

Table 2 describes the columns of data provided in the catalogs of this data release. The positions reported for sources correspond to the coordinates of the IRAC sources that were used as priors for the photometric measurements in the 24 to 500  $\mu\text{m}$  bands. These IRAC coordinates are calibrated to match the GOODS ACS version 2 coordinate system.<sup>2</sup> Only sources with  $\geq 3\sigma$  detections at 24  $\mu\text{m}$  are reported in the catalog. For sources that are not individually detected in the far-infrared images, we report the local noise level at the position of the source (i.e.,  $\sigma^{ima}$ ). These local noise estimates can be used to compute upper flux limits for non-detections. If the source position is not covered by the far-infrared images, then  $\sigma^{ima}$  is not computed. Uncertainties derived using our Monte-Carlo simulations are only provided for sources situated in the region of the field with relatively deep and homogeneous exposure times, i.e., the region in which our Monte-Carlo simulations have been carried out. For each IRAC position we give the corresponding exposure time of our mid- or far-infrared images. At 24  $\mu\text{m}$  and 70  $\mu\text{m}$  (*Spitzer*-MIPS) it corresponds to seconds/pixel. At 100, 160, 250, 350 and 500  $\mu\text{m}$  (*Herschel*) it corresponds to the number of detector pixels that have contributed to the value of the pixel in the final projected image. Because *Herschel* scans the sky at constant speed, this number of 'detector pixels' is proportional to the exposure time in seconds/'projected image pixels'.

For convenience, we include flux information from the four *Spitzer* IRAC channels for the mid- and far-infrared sources reported in this catalog. The IRAC fluxes were measured within an aperture diameter of 4 arcsec, and scaled to total flux using fixed aperture correction factors determined from Monte Carlo simulations by inserting artificial sources into the images and then measuring their fluxes with SExtractor. The simulations were done for compact galaxy profiles with intrinsic half-light radius  $\leq 0.5$  arcsec, which means that they are essentially unresolved by IRAC. The derived multiplicative aperture correction factors are 1.339, 1.393, 1.652, and 1.866 for IRAC channels 1 to 4, respectively. In practice, some of the brighter galaxies, especially at low redshifts, are resolved in the IRAC images, and the aperture corrected fluxes will therefore be underestimated. The IRAC flux uncertainties reported here are *purely* derived from the background noise in the images, measured directly from the data using split-image difference tests. These uncertainties would be correct for an isolated IRAC source, but do *not* include any terms to account for the effects of confusion or source blending. These are therefore minimum values and will likely underestimate the uncertainties for many sources, particularly those with close neighbors.

The catalog also includes IRAC source extraction flags, which are derived from the IRAC flag maps as described in the GOODS project DR1 documentation<sup>3</sup>. The IRAC

<sup>2</sup>see the GOODS ACS data release at MAST, <http://archive.stsci.edu/prepds/goods/>

<sup>3</sup>See the GOODS *Spitzer* first data release at: [http://irsa.ipac.caltech.edu/data/GOODS/docs/goods\\_dr1.html](http://irsa.ipac.caltech.edu/data/GOODS/docs/goods_dr1.html)

flag maps set bit values corresponding to various conditions, described in Table 2. The flag values in the catalog are computed from a logical ‘OR’ operation over the flag map values for all pixels within the SExtractor segmentation map for each object. The flag values often appear in combination. For example, regions with  $< 20\%$  of the modal exposure time (flag value 2) also have  $< 50\%$  of the modal exposure time (flag value 1). Therefore, those sources will have flag values of  $2 + 1 = 3$ . Regions with no data will have flag values  $64 + 2 + 1 = 67$ . Regions with residual muxbleed (flag 16) that also fall in a region with  $< 50\%$  modal exposure time (flag 1) will have flag  $16 + 1 = 17$ .

## 7 References

Berta et al. 2010, A&A, 518, 30 • Berta et al. 2011, A&A, 532, 49 • Elbaz et al. 2011, A&A, 533, 119 • Elbaz et al. 2010, A&A, 518, L29 • Frayer et al. 2006, ApJ, 647, L9 • Fruchter & Hook 2002, PASP, 114, 144 • Hwang et al. 2010, MNRAS, 409, 75 • Lutz et al. 2011, A&A, 532, A90 • Magdis et al. 2011, A&A, 534, 15 • Magnelli et al. 2009, A&A, 496, 57 • Magnelli et al. 2011, A&A, 528, 35 • Oliver et al. 2010, A&A, 518, 21 • Papovich et al. 2004, ApJS, 154, 70 • Pilbratt et al. 2010, A&A, 518, 1 • Starck & Murtagh 1998, PASP, 110, 193 • Wieprecht et al. 2009, ASPC, 411, 531

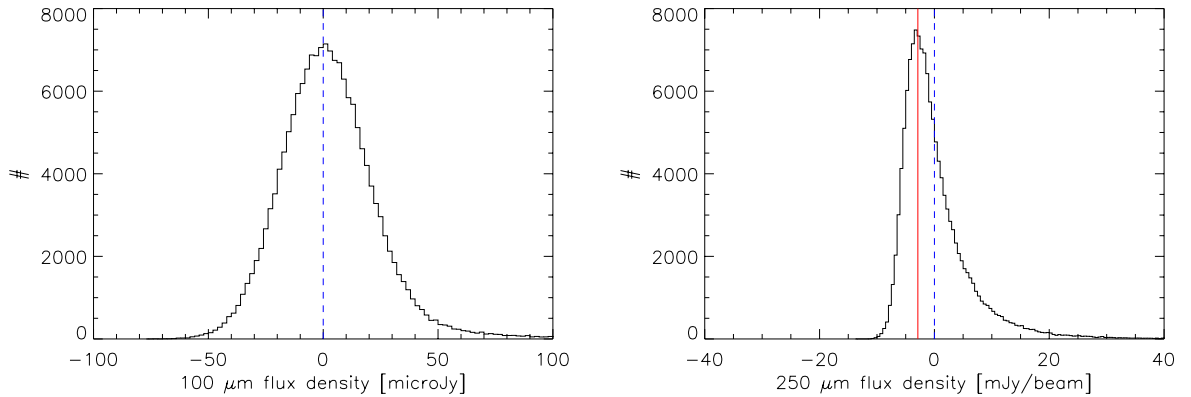


Figure 1: Histograms of pixel values in GOODS-N for the PACS  $100\ \mu\text{m}$  and SPIRE  $250\ \mu\text{m}$  mosaics. Pixel values were multiplied by  $10^6$  for PACS and  $10^3$  for SPIRE. The histogram of SPIRE pixel intensities peaks at a negative value because a constant mean level is subtracted from the data during standard map-making procedures.

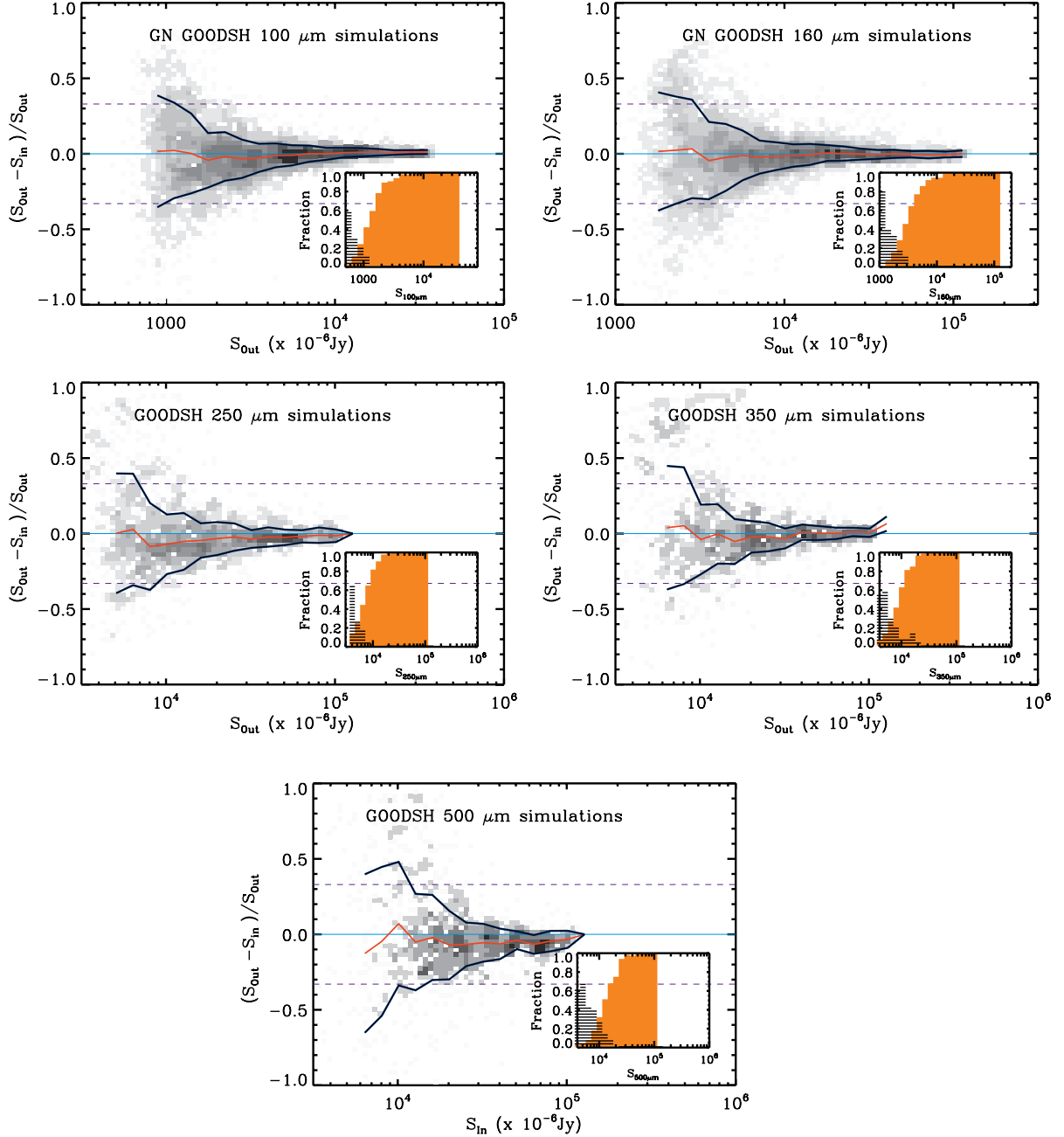


Figure 2: Results of Monte-Carlo simulations of source extraction in the GOODS-N field. The red lines represent the average photometric accuracy while the blue lines indicate the standard deviation observed in each flux bin (after  $3\sigma$  clipping). Inset plots show the fraction of artificial sources detected in the image (completeness) as a function of input flux (*orange plain histogram*) and the fraction of *spurious* sources (contamination) as a function of flux density (*striped black histogram*). For the definition of the completeness and contamination see the text.

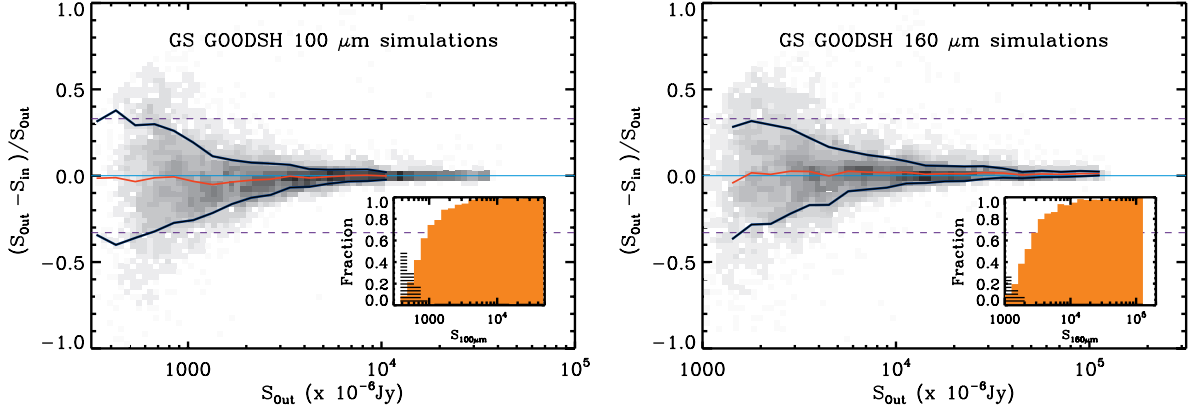


Figure 3: Results of the Monte-Carlo simulations in the GOODS-S field. Lines and symbols are the same as in Figure 2

Table 1: Statistics of our released catalogs

Field & bands	Min. coverage $\propto$ s/pixel	$1\sigma^{ima}$ mJy	$1\sigma^{sim}$ mJy	Completeness $3\sigma^{sim}$	Contamination $3\sigma^{sim}$	S(80%) mJy
GN 24	9500	0.003	0.007	40%	15%	0.030
GN 70	9000	0.3	0.66	50%	15%	2.5
GN 100	150	0.36	0.35	42%	12%	1.7
GN 160	150	0.80	0.84	32%	16%	5.5
GN 250	620	1.98	2.13	40%	15%	10
GN 350	700	2.48	2.56	44%	18%	13
GN 500	760	3.54	4.13	51%	13%	22
GS 24	9500	0.003	0.007	40%	15%	0.030
GS 70 deep	9000	0.3	0.66	50%	15%	2.5
GS 70 shallow	6000	0.4	0.83	45%	15%	3.5
GS 100	400	0.26	0.26	42%	17%	1.3
GS 160	400	0.60	0.67	38%	9%	3.9

The second column gives the minimum threshold in exposure time or map coverage value used to define the regions over which Monte Carlo artificial object simulations were carried out to derive the uncertainty  $\sigma^{ima}$  and the completeness and contamination levels. The adopted definition of completeness and contamination is described in the text, and reported here at flux levels equal to  $3\sigma^{ima}$ . The last column gives the flux level at which the catalogs are 80% complete.

Table 2: IRAC flag values

Flag value	Condition
0	>50% of the modal exposure time
1	<50% of the modal exposure time
2	<20% of the modal exposure time
16	Region with significant residual muxbleed artifacts
64	No data (zero retained exposure time)

Flag values often appear in combination. An object with < 20% of the modal exposure time also has < 50% of the modal exposure time, and thus flag = 2 + 1 = 3. Objects with no data in one IRAC band have flag values 64 + 2 + 1 = 67.

## FORMAT OF THE RELEASED GOODS-N/S\* catalogs

```
# ID_IAU          IAU coded object identification
# id sequential id
# ra IRAC measured ra
# dec IRAC measured dec
# F3p6 3.6um flux density in uJy
# err3p6 3.6um flux error
# flag3p6 3.6 source extraction flag
# F4p5 4.5um flux density in uJy
# err4p5 4.5um flux error
# flag4p5 4.5 source extraction flag
# F5p8 5.8um flux density in uJy
# err5p8 5.8um flux error
# flag5p8 5.8 source extraction flag
# F8p0 8.0um flux density in uJy
# err8p0 8.0um flux error
# flag8p0 8.0 source extraction flag
# F24 Spitzer MIPS 24um flux density in uJy
# err24_ima Spitzer MIPS 24um flux error residual map
# err24_sim Spitzer MIPS 24um flux error Monte-Carlo simulations
# cov24 Spitzer MIPS 24um coverage map value (equal to sec/pixel)
# F70 Spitzer MIPS 70um flux density in uJy
# err70_ima Spitzer MIPS 70um flux error residual map
# err70_sim Spitzer MIPS 70um flux error Monte-Carlo simulations
# cov70 Spitzer MIPS 70um coverage map value (equal to sec/pixel)
# F100 Herschel PACS 100um flux density in uJy
# err100_ima Herschel PACS 100um flux error residual map
# err100_sim Herschel PACS 100um flux error Monte-Carlo simulations
# cov100 Herschel PACS 100um coverage map value (proportional to sec/pixel)
# F160 Herschel PACS 160um flux density in uJy
# err160_ima Herschel PACS 160um flux error residual map
# err160_sim Herschel PACS 160um flux error Monte-Carlo simulations
# cov160 Herschel PACS 160um coverage map value (proportional to sec/pixel)
# F250 Herschel SPIRE 250um flux density in uJy
# err250_ima Herschel SPIRE 250um flux error residual map
# err250_sim Herschel SPIRE 250um flux error Monte-Carlo simulations
# cov250 Herschel SPIRE 250um coverage map value (proportional to sec/pixel)
# F350 Herschel SPIRE 350um flux density in uJy
# err350_ima Herschel SPIRE 350um flux error residual map
# err350_sim Herschel SPIRE 350um flux error Monte-Carlo simulations
# cov350 Herschel SPIRE 350um coverage map value (proportional to sec/pixel)
# F500 Herschel SPIRE 500um flux density in uJy
# err500_ima Herschel SPIRE 500um flux error residual map
# err500_sim Herschel SPIRE 500um flux error Monte-Carlo simulations
# cov500 Herschel SPIRE 500um coverage map value (proportional to sec/pixel)
# CLEAN_INDEX index measuring flux contamination from nearby sources
```

\* The GOODS-S catalog has no SPIRE measurements